Coupling of Li motion and structural distortions in olivine $LiMnPO_4$ from ^7Li and ^{31}P NMR

Christian Rudisch,[1] Hans-Joachim Grafe,[1] Jochen Geck,[1] Sven Partzsch,[1] M. v. Zimmermann,[2] Nadja Wizent,[1,3] Rüdiger Klingeler,[3] and Bernd Büchner[1]

[1]*IFW Dresden, Leibniz Institute for Solid State and Materials Research, D-01171 Dresden, Germany*

[2]*Deutsches Elektronen-Synchrotron DESY, D-22603 Hamburg, Germany*

[3]*Kirchhoff-Institut für Physik,Universität Heidelberg, D-69120 Heidelberg, Germany*

(Received 23 April 2013; revised manuscript received 17 July 2013; published 26 August 2013)

We present a detailed ^7Li- and ^{31}P-NMR study on single crystalline $LiMnPO_4$ in the paramagnetic and antiferromagnetic phase (AFM, $T_N \sim 34$ K). This allows us to determine the spin directions in the field-induced spin-flop phase. In addition, the anisotropic dipolar hyperfine coupling tensor of the ^7Li and ^{31}P nuclei is also fully determined by orientation and temperature-dependent NMR experiments and compared to the calculated values from crystal structure data. Deviations of the experimental values from the theoretical ones are discussed in terms of Mn disorder which is induced by Li disorder. In fact, the disorder in the Mn sublattice is directly revealed by diffuse x-ray scattering data. The present results provide experimental evidence for the Li diffusion strongly coupling to structural distortions within the $MnPO_4$ host, which is expected to significantly affect the Li mobility as well as the performance of batteries based on this material.

DOI: 10.1103/PhysRevB.88.054303 PACS number(s): 66.30.H−, 82.47.Aa, 76.60.−k, 61.05.cp

I. INTRODUCTION

Since the pioneering work of Padhi *et al.*[1] in 1997, phospho-olivine materials have been highly interesting for an application in rechargeable lithium batteries. $LiMnPO_4$ is a member of the olivine type lithium phosphate family and features several advantages regarding battery technology such as excellent chemical and thermal stability, nontoxicity in contrast to $LiCoO_2$, and economic viability and availability of the raw materials.[2–4] Despite these clear advantages of $LiMnPO_4$ for battery applications, there are also reports about its poor electrochemical performance.[1,5–7] The reasons for this currently remain unclear, but it has been found that $LiMnPO_4$ incorporated in carbon-coated nanostructures provides a competitive next generation cathode material with a stable reversible capacity up to 145 mAh/g and a rather flat discharge voltage curve at 4.1 V.[8–10]

Besides its relevance for battery applications $LiMnPO_4$ also exhibits interesting magnetic properties. More specifically, applying a magnetic field leads to a spin-flop phase with a slight ferromagnetic canting, which could exhibit magnetoelectric effects.[11] In addition, in $LiMPO_4$ with $M =$ Co or Ni unusual ferrotoroidic domains have been discovered.[12]

In this paper we address the origin of the poor electrochemical performance of $LiMnPO_4$ as well as the possible magnetoelectric effect in this material. To this end, we performed full orientation and temperature-dependent ^7Li and ^{31}P NMR experiments on a single crystal of $LiMnPO_4$. This allowed us to determine the complete dipolar hyperfine coupling tensor $\hat{A}_{\mathrm{dip}}$, which is compared to the calculated one from the positions of the atoms in the unit cell. Deviations of the experimentally obtained hyperfine coupling tensors from the calculated tensors and an anomalous broadening of the resonance lines in the paramagnetic phase are discussed in terms of Mn disorder in the samples. The conclusions from NMR are corroborated by our diffuse x-ray-diffraction (XRD) experiments, which directly reveal the disorder in the Mn sublattice. The NMR spectra in the AFM phase have been measured at 4.2 K, and the number of resonance lines agrees with the calculated spectra. Furthermore, the spectra allowed us to determine the spin directions in the spin-flop phase as well as the tilt of the spins due to the applied external magnetic field, which is important in order to assess the possible magnetoelectric effect in this material.

Our findings of Mn disorder in $LiMnPO_4$ provide firm experimental evidence that the movement of Li within $LiMnPO_4$ is strongly coupled to the lattice. Certainly, this also affects the mobility of the Li in $LiMnPO_4$, and therefore the performance of this material as a battery. Interestingly, our results are perfectly consistent with a recent theoretical study which found a formation of a vacancy-polaron complex by a lithium vacancy and a corresponding hole polaron at the fully lithiated limit owing to lattice distortion and Coulomb interaction between them,[5] thereby explaining the poor electrochemical performance of $LiMnPO_4$ if non-carbon-coated microstructures or single crystals are considered.

II. EXPERIMENTAL DETAILS

A. Sample preparation and characterization

The single crystal investigated in this work was grown at the IFW Dresden by the floating-zone method.[13,14] A phase pure single crystalline grain of the approximate size of $2 \times 2 \times 4$ mm was cut out of the grown rod. The phase purity was checked by x-ray-diffraction measurement, and the stoichiometry of the sample was determined by ICP-OES (inductively coupled plasma optical emission spectroscopy), which yields 4.3% Li, 35.4% Mn, and 60.3% PO_4 with a standard deviation of ±0.3% in agreement with the nominal composition. The crystal structure of $LiMnPO_4$ shown in Fig. 1 belongs to the *Pnma* space group. The Mn atoms are surrounded by distorted octahedra of oxygen atoms. The P atoms are tetrahedrally surrounded by oxygen atoms forming PO_4^{3-} groups.[15] There are four Li and four P positions which are crystallographically equivalent. The Mn ions are in a Mn^{2+} state resulting in a spin of $S = 5/2$ and an effective magnetic moment of $5.9\mu_B$.[13] The Mn magnetic moments

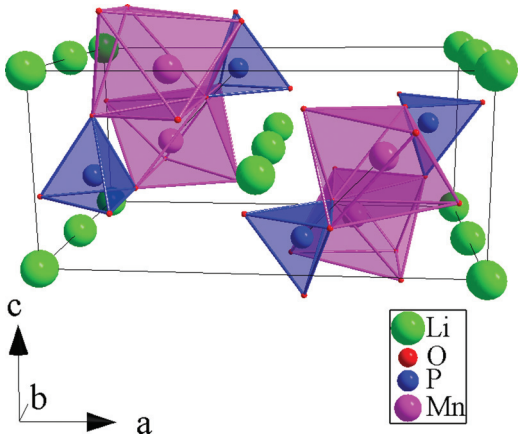

FIG. 1. (Color online) Crystal structure of $LiMnPO_4$. The crystallographic axes (a, b, and c) are along the edges of the unit cell. The slightly distorted MnO_6 octahedra (shaded in violet) share the oxygen anions with the PO_4 tetrahedra (shaded in blue).

align antiferromagnetically below $T_N \sim 34$ K (Ref. 13) along the a axis.[16]

B. NMR and hyperfine coupling tensor

NMR is an ideal tool to study both the Li diffusion process, which is important for application in lithium ion batteries, as well as the local magnetic properties. The Li diffusion process determines the mobility of the Li ions in a material and can be investigated by ^{7}Li-NMR linewidth and spin lattice relaxation measurements,[17,18] while the magnetism can be probed by any nucleus in the material that is coupled to the magnetic ion. For both processes, the detailed knowledge of the hyperfine coupling tensor between the electron spin and the nuclear probes—here the nuclear spins of ^{7}Li and ^{31}P—is helpful. However, since in $LiMnPO_4$ the spin lattice relaxation rate $T_1^{-1}$is dominated by the large magnetic moment of the Mn, the diffusion parameters cannot be determined by means of T_1^{-1}. Nevertheless, we measured T_1^{-1} of the ^{7}Li which agrees well with that in powder samples reported in the literature.[19]

All NMR experiments are done at a constant field of $H_0 = 7.0494$ T. For orientation-dependent NMR measurements a probe with a single axis goniometer was used which allows one to rotate the sample by a certain angle inside the magnet. The temperature-dependent NMR measurements were done in a temperature range from 4.2 up to 420 K. In the following, only the dipolar hyperfine coupling will be described in detail, since as we will see the other hyperfine couplings are either negligible (quadrupolar coupling, diamagnetic, and orbital shift) or isotropic (Fermi contact from unpaired s electrons on the ^{31}P).

The Hamiltonian describing the dipolar coupling of the nuclear spin to the Mn electronic spins is expressed by

$$\mathcal{H}_{\rm dip} = \hbar\gamma_n B_{\rm dip} = -\frac{\mu_0}{4\pi}\gamma_e\gamma_n\hbar^2 \sum_j \vec{I}\cdot\hat{A}_{{\rm dip},j}\cdot\vec{S}_j^T. \qquad (1)$$

Here, $B_{\rm dip}$ represents the dipolar field of the electronic spin located at the Mn site. γ_n corresponds to the gyromagnetic ratio of the nuclei ^{7}Li and ^{31}P ($\gamma_{\rm Li} = 16.5461$ MHz, $\gamma_{\rm P} = 17.2347$ MHz). γ_e is the gyromagnetic ratio of the electron. The nuclear and jth electron spin are represented by $\vec{I}$ and $\vec{S}_j^T$, respectively. The anisotropic dipolar coupling between the nuclear and the electron spins is described by the dipolar hyperfine coupling tensor $\hat{A}_{\rm dip}$ (see, e.g., Ref. 20). It has been calculated for the paramagnetic $\hat{A}_{\rm dip}^{\rm para}$ and AFM phase $\hat{A}_{\rm dip}^{\rm AFM}$ from the crystal structure data.

All electron spins within a sphere with a radius of 100 Å have been considered, leading to the same tensor elements A_{mn} of $\hat{A}_{\rm dip}$ as reported by Mays *et al.*[15] The different positions in the crystal of the ^{7}Li and the ^{31}P naturally lead to different dipolar hyperfine coupling tensors $\hat{A}_{\rm dip,Li}$ and $\hat{A}_{\rm dip,P}$, respectively. Crystallographically, there are four equivalent ^{7}Li and ^{31}P sites in the unit cell. However, for each nucleus, the diagonal elements A_{mm} of $\hat{A}_{\rm dip}$ are the same, whereas the off-diagonal elements $A_{mn}(m \neq n)$ are different. Therefore, for both nuclei, single resonance lines are expected for $H_0 \parallel a,b$, and c, whereas the different off-diagonal elements lead to a splitting of the resonance lines for angles off these high symmetry directions in the paramagnetic phase.

In the antiferromagnetically ordered state, the calculated hyperfine coupling $\hat{A}_{\rm dip,Li}^{\rm AFM}$ vanishes, i.e., no internal, dipolar field remains at the Li sites, leading to an unshifted single resonance line for the ^{7}Li. The experimental ^{7}Li resonance line, however, does yield a finite shift at 4.2 K, but tends toward zero. The calculation of $\hat{A}_{\rm dip,P}^{\rm AFM}$ leads to four magnetically inequivalent P sites in the AFM phase. Note that the diagonal elements of these P sites are different. Therefore, up to four ^{31}P-NMR lines are expected in the AFM phase. The calculated tensor elements of the paramagnetic and the AFM phase for ^{7}Li and ^{31}P nuclei are listed in Table I where a comparison of calculated and experimentally determined values is given.

C. X-ray-diffraction experiments

Complementary structural information has been obtained by high-energy x-ray-diffraction (HE-XRD) studies on the same single crystal. The experiments were performed at the beamline BW5 at the HASYLAB in Hamburg, using x rays with photon energies of 100 keV. Due to the large penetration depths at this energy ($\sim$1 mm), surface effects have no influence on the detected signal, ensuring the detection of real bulk properties. We performed triple-axis diffraction in horizontal Laue geometry utilizing the (111) reflection of a Si/Ge-monochromator and Si/Ge-analyzer crystal.

III. RESULTS AND DISCUSSION

A. NMR spectra and temperature dependence

In Fig. 2 the ^{7}Li- and ^{31}P-NMR spectra are shown for $H_0 \parallel a$, $H_0 \parallel b$, and $H_0 \parallel c$ at 292 K. Due to the anisotropy of the dipolar hyperfine couplings $\hat{A}_{\rm dip,Li}$ and $\hat{A}_{\rm dip,P}$ the resonance frequency ν is different for the different orientations.

The ^{7}Li-NMR spectra for all different orientations are spanning a frequency interval of 500 kHz at 292 K. This value agrees well with the full width of ^{7}Li-NMR spectra in $LiMnPO_4$ powder samples reported in Ref. 19. The linewidth shows a linear field dependence (e.g., $\Delta\nu(7\ T) \sim 80$ kHz, whereas $\Delta\nu(3\ T) \sim 40$ kHz). This indicates a dipolar broadening, where each ^{7}Li (^{31}P) nucleus sees a slightly different

TABLE I. Comparison of calculated and NMR determined tensor elements for the paramagnetic phase. The elements for the AFM phase are calculated. All elements are given in T/μ_B.

Nuclei	tensor element	Paramagnetic phase: Crystal structure (calculated)	Paramagnetic phase: NMR (experimental)	Paramagnetic phase: Residue	AFM phase: Crystal structure (calculated)
^{7}Li	$A_{11,\mathrm{Li}}$	0.0690	0.0717	0.0027	0
	$A_{22,\mathrm{Li}}$	−0.0401	−0.0198	0.0203	0
	$A_{33,\mathrm{Li}}$	−0.0289	−0.0430	−0.0141	0
	$A_{12,\mathrm{Li}}$	±0.0058			0
	$A_{13,\mathrm{Li}}$	±0.0030			0
	$A_{23,\mathrm{Li}}$	±0.0060			0
^{31}P	$A_{11,\mathrm{P}}$	0.0376	0.4429	0.4053	±0.0881
	$A_{22,\mathrm{P}}$	−0.0193	0.3847	0.4040	±0.1560
	$A_{33,\mathrm{P}}$	−0.0183	0.3710	0.3893	±0.0679
	$A_{12,\mathrm{P}}$	0			0
	$A_{13,\mathrm{P}}$	±0.0282	+0.0388/−0.0362	0.0106/0.0080	±0.0374
	$A_{23,\mathrm{P}}$	0			0

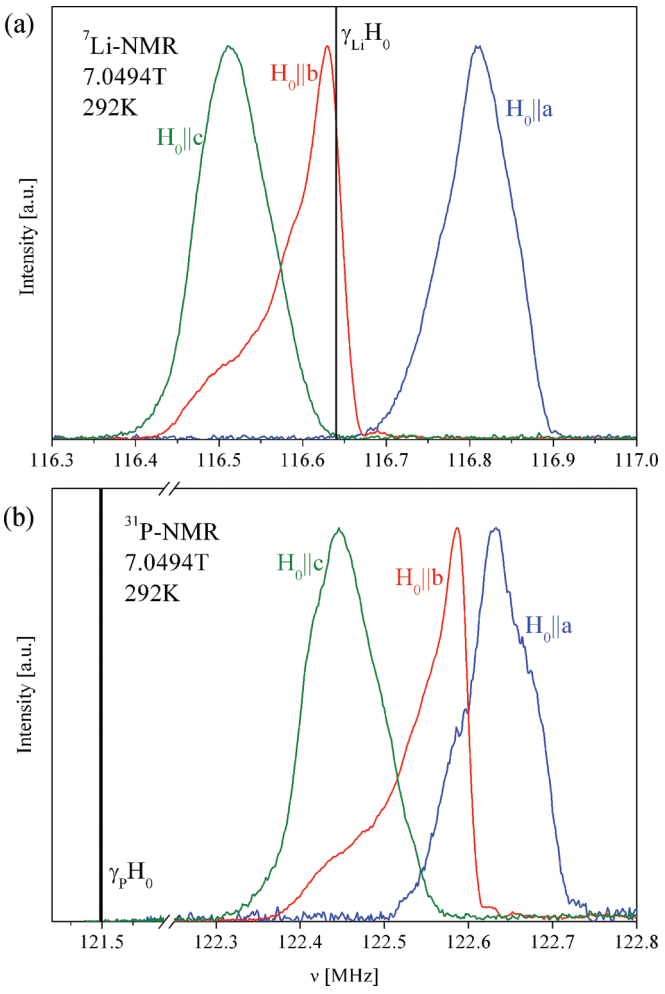

FIG. 2. (Color online) (a) ^{7}Li-NMR spectra and (b) ^{31}P-NMR spectra for the orientations $H_0\|a$, $H_0\|b$, and $H_0\|c$. The average linewidth is ∼80 kHz. The ^{7}Li-NMR spectra in (a) exhibit a small shift around the resonance line of a bare nucleus ($\gamma_{\mathrm{Li}}H_0$). The ^{31}P-NMR spectra in (b) are showing large shifts to higher resonance frequencies, which can be due to the isotropic contact interaction (see text).

dipolar hyperfine field of the Mn electronic spins. However, the asymmetric shape of the resonance lines (especially for $H_0\|b$) differs much from the expected Gaussian shape of a resonance line in a single crystal, indicating a substantial amount of disorder in the sample. For this reason, we have calculated the Knight shift of the ^{7}Li and ^{31}P from the center of gravity of the resonance lines, and the width $\Delta\nu$ of the spectra has been determined by the square root of the second moment.

Furthermore, a comparison of the resonance lines in Fig. 2 shows that for the corresponding orientations the shapes of ^{7}Li- and ^{31}P-NMR spectra are very similar. This indicates that the shape of the resonance lines of both nuclei must be affected by the same factor. If only the ^{7}Li is disordered in the crystal, this would not affect the ^{31}P resonance lines and vice versa.

A misalignment of the external field can be excluded, too, since the crystal was accurately oriented by making use of the angle dependence of the resonance frequencies of the ^{7}Li and ^{31}P resonance lines (see Figs. 5–7). A quadrupolar broadening or splitting of the ^{7}Li spectra ($I = 3/2$) could also not be observed, indicating a very small electric field gradient at the Li site. Therefore, the anomalous shape of the resonance lines of both nuclei must originate either from a distribution of local moments of the Mn, i.e., a distribution of the valence of the Mn, or a distribution of the hyperfine coupling which can originate from a site disorder of the Mn. Since there are no indications for a distribution of the Mn valence,[13] we conclude that there is substantial Mn site disorder. A detailed comparison of the calculated and experimental hyperfine coupling tensor elements in the following points in the same direction. Further investigations by diffusive x-ray scattering (see Sec. IV) corroborate the existence of Mn site disorder in $LiMnPO_4$.

The temperature dependence of the resonance frequencies for ^{7}Li and ^{31}P, $\nu(T)$, is shown in Figs. 3(a) and 3(b). In the paramagnetic phase, $\nu(T)$ can be described by

$$\nu(T) = \gamma_n H_0 \left[1 + A_{mm}\chi(T)\right], \tag{2}$$

where A_{mm} are the diagonal dipolar hyperfine coupling tensor elements for the corresponding orientations ($H_0\|a$, $H_0\|b$, $H_0\|c$, $m = 1,2,3$, respectively). The magnetic susceptibility

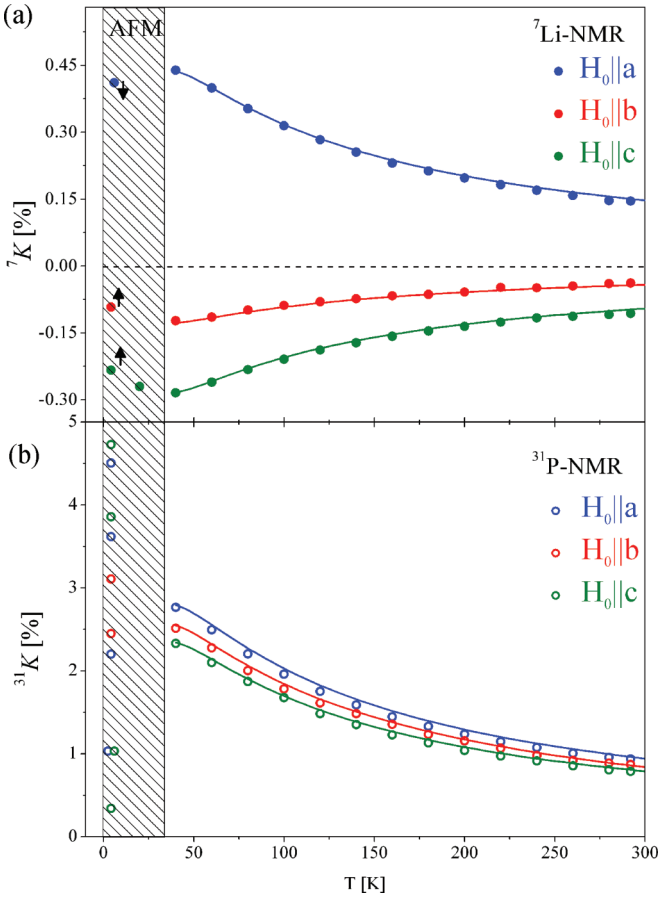

FIG. 3. (Color online) Temperature dependence of the Knight shift (a) ^7K and (b) ^{31}K for the orientations $H_0\|a$, $H_0\|b$, and $H_0\|c$ in the paramagnetic and AFM phases. The measured data are indicated by the dots. The solid lines correspond to the Knight shift which is calculated by $K = A^{\rm exp}_{mm}\chi(T)$ with $m = 1,2,3$ for $H_0\|a$, $H_0\|b$, and $H_0\|c$, respectively. The diagonal tensor elements $A^{\rm exp}_{mm}$ are determined from fits of Clogston-Jaccarino plots and listed in Table I. (a) The presence of the anisotropic dipolar coupling leads to positive and negative ^7K for corresponding orientation. In the AFM phase the single resonance line shifts towards $^7K = 0$, which is indicated by the arrows. (b) The superposition of the field caused by the contact term and the field of the dipolar coupling leads to a comparatively high ^{31}K. In the AFM phase four resonance lines are observed for $H_0\|a$ and $H_0\|c$ and two for $H_0\|b$.

is isotropic in the paramagnetic phase,[13] and thus $\chi(T)$ is a scalar in Eq. (2). From Clogston-Jaccarino plots the diagonal elements $A^{\rm exp}_{mm}$ are obtained for the corresponding orientations (see Table I). Since A_{22} and A_{33} for ^{7}Li are negative, the resonance lines for $H \parallel a$ and b shift to lower frequencies. For the ^{31}P, there is an additional temperature-dependent contact term [see Fig. 2(b)] which leads to a positive shift of the resonance frequency for all three directions. The contact term is also responsible for the large deviation of the calculated and experimentally determined coupling constants in Table I. Further deviations may arise from the anomalous shape of the spectra due to the Mn disorder.

The temperature dependence of the square root of the second moment $\Delta\nu$ of the ^{7}Li- and ^{31}P-NMR spectra is shown in Fig. 4. With decreasing temperature $\Delta\nu$ increases, which is

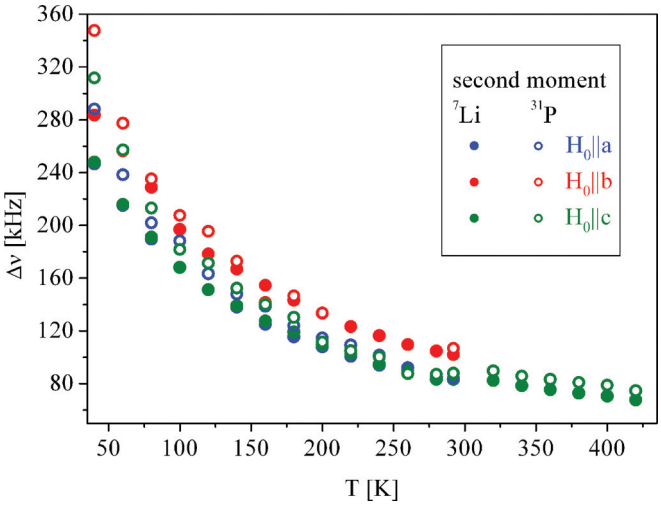

FIG. 4. (Color online) Comparison of the temperature-dependent second moment $\Delta\nu$ between ^{7}Li- and ^{31}P-NMR spectra. The second moment of the ^{31}Pspectra is almost always larger than the corresponding second moment of the ^{7}Li spectra. This effect is predominantly related to a distribution of internal fields by the contact interaction on the P nuclei. For $H_0\|c$ the spectra are measured up to 420 K, where the second moment remains almost constant at 80 kHz.

the expected behavior for magnetic broadening which scales with the susceptibility χ. For $H_0\|c$ the spectra were measured up to 420 K (see Fig. 4). Above $\sim$300 K, the second moment is almost constant yielding a value of $\Delta\nu \sim 80$ kHz. As can be seen in Fig. 4, $\Delta\nu$ of the ^{31}P-NMR spectra is slightly larger for the corresponding orientations than $\Delta\nu$ of the ^{7}Li. The reason for this could be a distribution of the hyperfine fields transferred by the contact interaction which affects only the ^{31}P, but not the ^{7}Li. The effect of the contact interaction is isotropic, hence the ^{31}P-NMR spectra are broadened without additional features in the shape of the resonance line.

B. Angle-dependent NMR frequencies

The full experimental orientation dependence of ^{7}Li and ^{31}P NMR can be described consistently with the susceptibility data and the hyperfine coupling tensor $\hat{A}^{\rm para}_{\rm dip}$.

The angle-dependent NMR data was obtained by rotating the crystal around the crystal axes from $H_0\|c$ to $H_0\|a$, from $H_0\|b$ to $H_0\|a$, and from $H_0\|b$ to $H_0\|c$ at 292 K. The angle dependence at this temperature can be described by

$$\nu(\phi,\theta) = \gamma_n H_0 \left[1 + \begin{pmatrix} \cos\phi\,\sin\theta \\ \sin\phi\,\sin\theta \\ \cos\theta \end{pmatrix} \times \hat{A}^{\rm para}_{\rm dip} \begin{pmatrix} \cos\phi\,\sin\theta \\ \sin\phi\,\sin\theta \\ \cos\theta \end{pmatrix} \chi(292\ {\rm K}) \right], \quad (3)$$

where the orientation of the crystal structure in the external field is expressed by the unit vectors given in spherical coordinates. The experimental and calculated data according to Eq. (3) are shown in Figs. 5–7. For the calculated curves the corresponding experimental diagonal elements and the calculated off-diagonal elements are used. The splitting of the

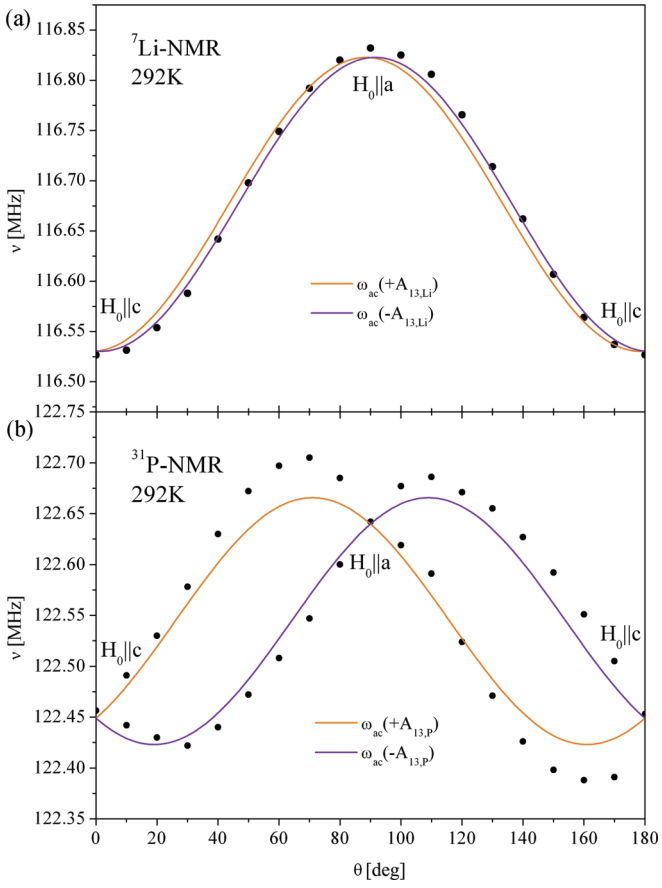

FIG. 5. (Color online) Experimental orientation dependence of ^{7}Li and ^{31}P NMR between $H_0\|c$ and $H_0\|a$. Expected curves: $\nu_{ac} = \gamma_n H_0[1 + (A_{11}\sin^2\theta + 2A_{13}\sin\theta\cos\theta + A_{33}\cos^2\theta)\chi(292\text{ K})]$ for the corresponding ^{7}Li and ^{31}P tensor elements. The diagonal elements are experimental; A_{13} is calculated. (a) The absolute value of $\pm A_{13,\mathrm{Li}}$ is relatively small which leads to a small splitting of the ^{7}Li-NMR resonance line on the order of $\sim$10 kHz, which is not oberservable due to the broad resonance line of $\sim$100 kHz. (b) The line splitting of $\sim$200 kHz is observable. The calculated off-diagonal element $\pm A_{13,P}$ is $\sim$10 times larger than $\pm A_{13,\mathrm{Li}}$, which increases the splitting in the ^{31}P-NMR spectrum.

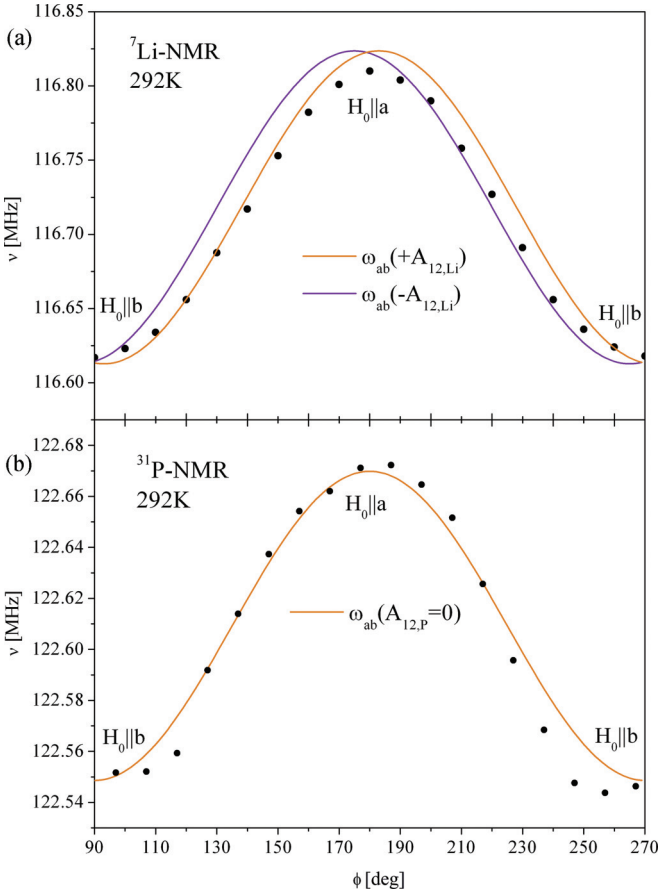

FIG. 6. (Color online) Experimental orientation dependence of ^{7}Li and ^{31}P NMR between $H_0\|b$ and $H_0\|a$. Expected curves: $\nu_{ab} = \gamma_n H_0[1 + (A_{11}\cos^2\phi + 2A_{12}\sin\phi\cos\phi + A_{22}\sin^2\phi)\chi(292\text{ K})]$. (a) $A_{12,\mathrm{Li}}$ causes the splitting on the order of $\sim$20 kHz, which is too small to observe it by ^{7}Li NMR because of the broad linewidth of $\sim$100 kHz. (b) $A_{12,P}$ vanishes (see Table I), which means that no splitting is present.

resonance lines for angles off the high symmetry directions is caused by the different magnetic ^{7}Li and ^{31}P sites (see Table II). The different sites lead to positive and negative signs of the off-diagonal elements A_{12}, A_{13}, and A_{23}.

In Fig. 5(a) the ^{7}Li-NMR spectrum shows a single resonance line in contrast to the ^{31}P-NMR spectrum in Fig. 5(b) which shows two resonance lines for angles off $H_0\|a$ and $H_0\|c$. From a comparison of the angle-dependent ^{31}P-NMR data reported in Ref. 15 and Fig. 5(b) the crystal axes a and c are confirmed. For rotating between $H_0\|c$ and $H_0\|a$, Eq. (3) simplifies to an equation which includes only the tensor elements A_{11}, A_{33}, and A_{13}. The absolute value of A_{13} determines the size of splitting that means the difference between the violet and orange curve in Fig. 5. In the ^{7}Li-NMR spectra the $A_{13,\mathrm{Li}}$ element leads to a splitting on the order of $\sim$10 kHz, which is completely covered by the broad linewidth of $\sim$100 kHz. The value $A_{13,\mathrm{P}}$ for ^{31}P is $\sim$10 times larger than $A_{13,\mathrm{Li}}$ (see Table I) and leads to a splitting of 200 kHz, which can be nicely observed in the ^{31}P-NMR spectra. Fitting the experimental ^{31}P-NMR orientation-dependent data in Fig. 5(b) leads to experimental values for $A_{13,\mathrm{P}}$ (see Table I).

The experimental results for rotating the crystal between $H_0\|b$ and $H_0\|a$ are shown in Fig. 6. For these orientations Eq. (3) simplifies to an equation including only A_{11}, A_{22}, and A_{12}. For this case A_{12} determines the size of the splitting.

The orientation dependence between $H_0\|b$ and $H_0\|c$ is shown in Fig. 7. Here, Eq. (3) includes only the tensor elements A_{22}, A_{33}, and A_{23}. In this case the off-diagonal element A_{23} is responsible for the splitting.

C. Discussion of the angle dependence

The angle dependence of the NMR spectra provides another indication that the broad lines and anomalous shape of the resonance lines in Fig. 2 are due to Mn disorder, and not due to differently oriented domains of the crystal. First of all, the angle dependencies of the ^{7}Li and the ^{31}P are completely different, but the shapes of the spectra are very similar. This can be seen in Fig. 5: whereas the ^{31}P lines split depending on

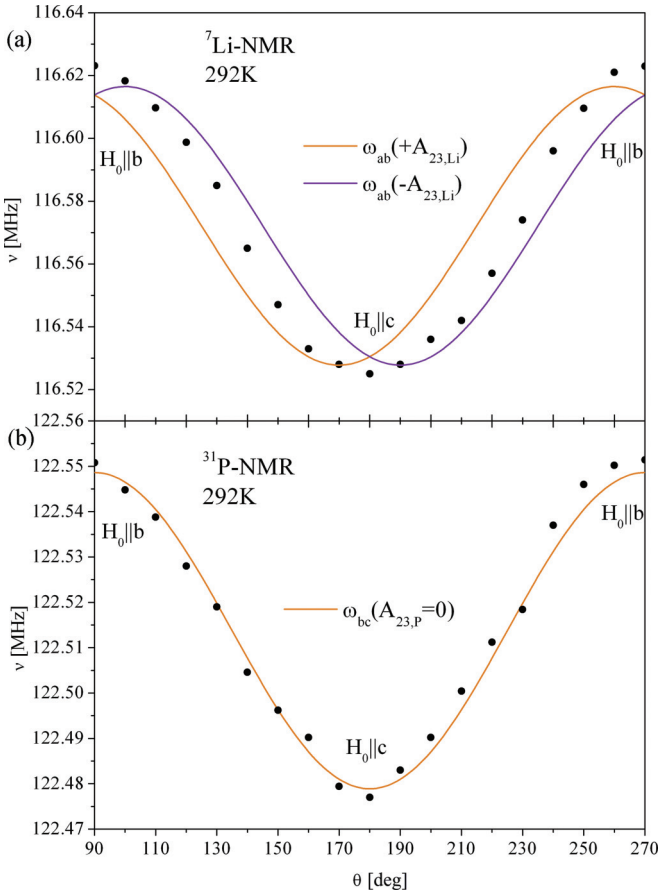

FIG. 7. (Color online) Experimental orientation dependence of ^{7}Li and ^{31}PNMR between $H_0\|b$ and $H_0\|c$. Expected curves: $\nu_{bc} = \gamma_n H_0[1 + (A_{22}\sin^2\theta + 2A_{23}\sin\theta\cos\theta + A_{33}\cos^2\theta)\chi(292\text{ K})]$. (a) $A_{23,Li}$ causes the splitting on the order of ∼30 kHz, which is too small to observe by ^{7}Li NMR because of the broad linewidth of ∼100 kHz. (b) $A_{23,P}$ vanishes (see Table I), which means that no splitting is present.

the angle θ, the ^{7}Li lines do not. In contrast, the shape of the spectra for $H_0\|a$ in Fig. 2 is very similar for both isotopes. An angle dependence as that of the ^{31}P in Fig. 5(b) would clearly lead to a different shape of the spectrum compared to the ^{7}Li. Similar arguments hold for the other two directions. Especially for $H_0\|b$, the shape of the spectra for ^{7}Li and ^{31}P are very similar, but the angle dependencies in Figs. 6 and 7 are not. For example, in Fig. 6, the difference of the resonance frequency of the ^{7}Li for $H_0\|a$ and $H_0\|b$ is ∼200 kHz, whereas it is only ∼120 kHz for the ^{31}P. In contrast, the distance between the shoulder and the peak for $H_0\|b$ in Fig. 2 is very similar for both isotopes, if not even larger for the ^{31}P. The same argument is true for the linewidths in general: The angle-dependent splitting is always larger for the ^{7}Li, whereas the FWHM tends to be larger for the ^{31}P. A broadening from differently oriented domains of a crystal would lead to the opposite trend, as can be deduced from the angle-dependent measurements.

Furthermore, the comparison of the calculated and experimental tensor elements indicates the presence of an additional hyperfine interaction for the ^{31}P nuclei. For the ^{7}Li the value of the diagonal element $A_{11,Li}$ determined by NMR and the value determined from the crystal structure agree, whereas the values for $A_{22,Li}$ and $A_{33,Li}$ are showing residues. The difference can be explained by the asymmetric shape of the resonance line for $H_0\|b$, which is most likely due to the Mn disorder. The calculation of the resonance frequency from the center of gravity therefore leads to a smaller shift of the resonance frequency than expected from the calculated $A_{22,Li}$. The residue of $A_{33,Li}$ possibly arises from the Mn disorder, too. Therefore, it can be concluded that the Mn disorder has its largest influence in the b and c directions because of the larger discrepancies of $A_{22,Li}$ and $A_{33,Li}$ compared to $A_{11,Li}$. A small displacement of some of the Mn atoms from their original positions in the lattice leads to a distribution of the dipolar hyperfine couplings resulting in the broad lines and the asymmetric shape. Note that the off-diagonal elements for ^{7}Li can, in principle, be determined, too. However, the splitting is only very small (∼10−40 kHz), and therefore cannot be resolved within the broad resonance lines (width ∼100 kHz).

In contrast to the ^{7}Li, the comparison of the experimental and calculated *diagonal* hyperfine coupling elements for the ^{31}P shows large residues (see Table I). Such a discrepancy

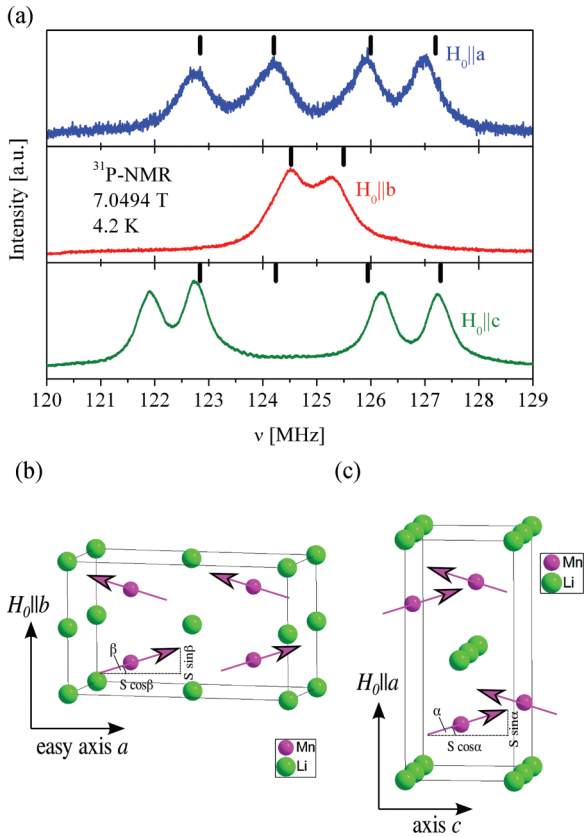

FIG. 8. (Color online) (a) ^{31}P-NMR spectra for $H_0\|a$, $H_0\|b$, and $H_0\|c$ at 4.2 K. By assuming tilt angles, the ^{31}P-NMR frequencies can be calculated as shown in Table III. The best match of experimental and calculated frequencies is achieved for $\alpha = 11°$, $\beta = 4°$, and $\gamma = 13°$. The calculated frequencies are indicated by the short black lines. (b) Tilts of the electronic spins in the AFM state. Exemplified shown for tilts in the b direction. For tilts in the c direction (tilt angle γ) the situation is similar. (c) Tilts in the SF state in the direction of a by the angle α. The tilt causes an additional component of the spins in field direction.

TABLE II. The signs for the off-diagonal elements of the magnetic unequal ^{7}Li and ^{31}P sites are shown. The sites are given in fractional coordinates.

^{7}Li sites	$A_{12,\mathrm{Li}}$	$A_{13,\mathrm{Li}}$	$A_{23,\mathrm{Li}}$	^{31}P sites	$A_{13,\mathrm{P}}$
(0/0/0)	+	+	−	(0.907/0.75/0.591)	−
(0/0.5/0)	−	+	+	(0.092/0.25/0.408)	−
(0.5/0/0.5)	+	−	+	(0.407/0.75/0.906)	+
(0.5/0.5/0.5)	−	−	−	(0.592/0.25/0.094)	+

has already been reported in Ref. 15 and has been explained by nondipolar hyperfine interactions of the ^{31}P nucleus with unpaired 3*s* (contact interaction) and/or 3*p* (core polarization) electrons of the phosphorous. These unpaired *s* and *p* electrons arise from the Mn-O-P-O-Mn superexchange path which is responsible for the interlayer magnetic coupling.[16] The difference between the experimental and calculated resonance frequencies of the ^{31}P NMR corresponds to an isotropic difference in the diagonal elements of the hyperfine coupling tensor of 0.4 T/μ_B, which underlines the isotropic character which is typical for a contact interaction.

The off-diagonal element $A_{13,\mathrm{P}}$ is causing a splitting of $\sim$200 kHz for angles between $H_0 \| a$ and $H_0 \| c$, which is larger than the averaged linewidth and therefore observable by ^{31}P NMR. From the obtained data the value of $A_{13,\mathrm{P}}$ with positive and negative signs is extracted by fitting both angle-dependent ^{31}P-NMR curves in Fig. 5(b) by using Eq. (3). The experimental absolute values of $\pm A_{13,\mathrm{P}}$ are slightly larger. The deviations may arise from the Mn disorder.

D. NMR in the antiferromagnetic phase

In order to check the dipolar coupling and to investigate the influence of the spin flop (SF) on the NMR spectra, we measured the ^{7}Li and ^{31}P spectra in the AFM phase at 4.2 K. In the single crystal at hand, the spin-flop field at this temperature amounts to 3.9 T. The NMR spectra are shown in Fig. 8(a) for the orientations $H_0 \| a$, $H_0 \| b$, and $H_0 \| c$. In the AFM phase the bulk susceptibility cannot be used to calculate the resonance frequencies from the dipolar hyperfine coupling, because a part of the electron spins changes its orientation to the opposite direction. In zero external magnetic field, the electron spins align antiparallel along the crystallographic *a* axis. For the NMR experiments, a strong external field $H_0 = 7$ T has been applied which leads to a tilt of the electron spins for the directions $H_0 \| b$ and $H_0 \| c$ by the angles β and γ, respectively, and to a spin-flop transition plus an additional tilt by the angle α for the direction $H_0 \| a$ [see Figs. 8(b) and 8(c)]. The occurrence of a spin-flop transition, possibly magnetoelectric in nature, has been reported in Refs. 11 and 21 for $H_0 > 4$ T parallel *a*. The tilt angle in the spin-flop phase is labeled α.

Equation (4) considers the additional fields induced by the contact interaction B_c and the dipolar field $B_{\mathrm{dip}}^{\mathrm{AFM}}$ which stems from the antiferromagnetic order of the electron spins.

$$\nu = \gamma_n \left(H_0 + B_c + B_{\mathrm{dip}}^{\mathrm{AFM}} \right). \tag{4}$$

The dipolar field $B_{\mathrm{dip,Li}}^{\mathrm{AFM}}$ vanishes for the ^{7}Li sites in the AFM phase, therefore the ^{7}Li-NMR spectra show a single resonance line at the frequency of a bare nucleus. In Fig. 3(a) the expected behavior is experimentally indicated by small shifts of the ^{7}Li-NMR resonance frequencies in the direction of the unshifted frequency at 4.2 K. The incomplete shifting to $\gamma_{\mathrm{Li}} H_0$ can be explained by a remaining dipolar field induced by the tilted electron spins.

The resonance lines in the AFM phase of the ^{31}P are shown in Fig. 8(a) for the orientations $H_0 \| a$, $H_0 \| b$, and $H_0 \| c$. The number of resonance lines in the ^{31}P-NMR spectra equals the number of different calculated dipolar fields $B_{\mathrm{dip,P}}^{\mathrm{AFM}}$ (see Table III).

The additional component in the field direction due to the tilt of the electronic spins is considered in Table III for the corresponding orientations. Then, the ^{31}P-NMR frequencies are calculated as a function of the tilt angles. The best match of experimental and calculated resonances are found for $\alpha = 11^\circ$, $\beta = 4^\circ$, and $\gamma = 13^\circ$. The calculated frequencies are indicated by bars in Fig. 8. For $H_0 \| a$ and $H_0 \| b$ the experimental and calculated resonance frequencies agree quite well, and the

TABLE III. The mathematical description for the orientations of $\vec{I}$ and $\vec{S}_j^T$ in the AFM phase is given in the second column. The result is shown in the third column. The number of different $B_{\mathrm{dip,P}}^{\mathrm{AFM}}$ is obtained from the combination possibilities of the ± sign of the tensor elements in the third column. The number of different dipolar fields $B_{\mathrm{dip,P}}^{\mathrm{AFM}}$ equals the number of experimental ^{31}P-NMR resonance lines. The tilt angles α, β, γ are defined in Figs. 8(b) and 8(c).

	$\vec{I}\cdot$	$\hat{A}_{\mathrm{dip,P}}^{\mathrm{AFM}}$	$\cdot\vec{S}^T$	$B_{\mathrm{dip,P}}^{\mathrm{AFM}} \propto \sum_j (\vec{I} \cdot \hat{A}_{j,\mathrm{P}}^{\mathrm{AFM}} \cdot \vec{S}_j^T)$	Number of different $B_{\mathrm{dip,P}}^{\mathrm{AFM}}$
$H_0 \| a$	$\begin{pmatrix} \frac{1}{2} \\ 0 \\ 0 \end{pmatrix}$	$\begin{pmatrix} \pm A_{11} & 0 & \pm A_{13} \\ 0 & \pm A_{22} & 0 \\ \pm A_{13} & 0 & \pm A_{33} \end{pmatrix}$	$\frac{5}{2}\begin{pmatrix} \sin\alpha \\ 0 \\ \cos\alpha \end{pmatrix}$	$\frac{5}{4}[(\pm A_{11})\sin\alpha + (\pm A_{13})\cos\alpha]$	4
$H_0 \| b$	$\begin{pmatrix} 0 \\ \frac{1}{2} \\ 0 \end{pmatrix}$	$\begin{pmatrix} \pm A_{11} & 0 & \pm A_{13} \\ 0 & \pm A_{22} & 0 \\ \pm A_{13} & 0 & \pm A_{33} \end{pmatrix}$	$\frac{5}{2}\begin{pmatrix} \cos\beta \\ \sin\beta \\ 0 \end{pmatrix}$	$\frac{5}{4}(\pm A_{22})\sin\beta$	2
$H_0 \| c$	$\begin{pmatrix} 0 \\ 0 \\ \frac{1}{2} \end{pmatrix}$	$\begin{pmatrix} \pm A_{11} & 0 & \pm A_{13} \\ 0 & \pm A_{22} & 0 \\ \pm A_{13} & 0 & \pm A_{33} \end{pmatrix}$	$\frac{5}{2}\begin{pmatrix} \cos\gamma \\ 0 \\ \sin\gamma \end{pmatrix}$	$\frac{5}{4}[(\pm A_{13})\cos\gamma + (\pm A_{33})\sin\gamma]$	4

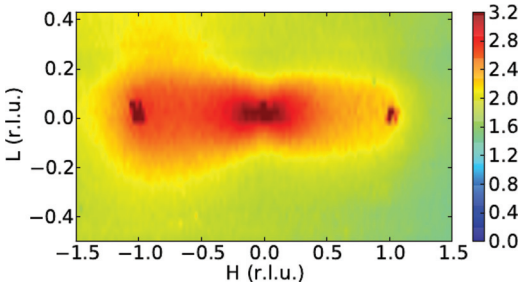

FIG. 9. (Color online) Diffuse scattering intensity around the forbidden (030) position. The intensity is given in counts/s at 100 mA ring current.

value for $H_0 \| a$ is also consistent with the tilt angle of 5.4° at $H_0 = 4.5$ T determined by neutron scattering[11] since the tilt angle of the spins almost depends linearly on the field. Only for $H_0 \| c$, the calculated resonances on the low-frequency side for some reason do not agree well with the experimental data.

IV. DIFFUSE X-RAY DIFFRACTION

The NMR line shape and angle dependence provide strong evidence for the presence of disorder of the Mn sublattice. In order to verify this conclusion we performed diffuse HE-XRD experiments on the same single crystals studied by NMR. The HE-XRD experiments were performed using a photon energy of 100 keV. At these energies the penetration depth of the x rays is of the order of millimeters, which guarantees the detection of true bulk properties and enables a direct comparison to the NMR results.

A representative data set is displayed in Fig. 9, where the diffuse scattering around the symmetry forbidden (030) is displayed. The very broad and diffuse HE-XRD intensity in the HL plane can clearly be observed. The strong diffuse scattering reveals significant structural disorder in the studied single crystals. The HE-XRD intensity is proportional to $(\mathbf{Q} \cdot \mathbf{d})^2$, where $\mathbf{Q}$ is the scattering vector and $\mathbf{d}$ represents the shift of a lattice site away from its ideal position. The diffuse scattering around $\mathbf{Q} = (0,3,0)$ therefore implies that the lattice disorder involves shifts parallel to the b axis, which are only very weakly correlated along a. The distribution of the diffuse intensity is also very anisotropic within the $(H3L)$ plane, i.e., the underlying disorder is anisotropic in real space, consitent with the NMR results. The data in Fig. 9 further implies that the symmetry of the ideal lattice is not strictly fulfilled and therefore the symmetry forbidden $(\pm 1,3,0)$ and $(0,3,0)$ reflections are also observed. In addition to this the HE-XRD intensity is dominated by the shifts of the heavy elements in the lattice. The results in Fig. 9 therefore directly reveal the disorder in the Mn sublattice and are in perfect agreement with the conclusions drawn from the NMR data.

Based on the available HE-XRD data, we cannot characterize the structural disorder in more detail. This is the subject of ongoing investigations.

V. CONCLUSIONS

We presented angle- and temperature-dependent ^{7}Li and ^{31}P NMR and diffuse x-ray-diffraction measurements in a $LiMnPO_4$ single crystal. The ^{7}Li- and ^{31}P-NMR resonance lines in the AFM and SF phase are consistent with the calculated resonances, when tilts of the magnetic moments in the direction of the external field are assumed. The broad ^{7}Li- and ^{31}P-NMR resonance lines in the paramagnetic phase indicate the existence of Mn site disorder. In combination with the susceptibility data the diagonal elements of the hyperfine coupling tensor are determined and compared with the values calculated from the crystal structure. The highest deviations show $A_{22,\mathrm{Li}}$ and $A_{33,\mathrm{Li}}$, which leads to the conclusion that the Mn disorder exists predominantly in the b and c directions. This is fully consistent with our HE-XRD data which indicates substantial Mn disorder along the b direction. Interestingly, recent theoretical results imply a strong coupling of the Li and the Mn sublattice in the fully lithiated limit.[5] The Mn disorder may hence be caused by the distribution of the mobile Li ions within the $MnPO_4$ host. Our finding of Mn disorder in $LiMnPO_4$ therefore provides experimental evidence that the movement of Li within $LiMnPO_4$ is significantly coupled to lattice distortions. Certainly, this will also affect the mobility of the Li in $LiMnPO_4$, and therefore the performance of this material as a battery.

ACKNOWLEDGMENTS

This research was financially supported by the DFG priority program SPP1473 (Grants No. GR3330/3-1 and No. KL1824/5). N.W. and R.K. acknowledge support by the BMBF via project 03SF0397. J.G. and S.P. gratefully acknowledge the financial support by the German Research Foundation through the Emmy-Noether program (Grant No. GE1647/2-1).

[1] A. K. Padhi, K. S. Najundaswamy, and J. B. Goodenough, J. Electrochem. Soc. **144**, 1188 (1997).
[2] Z. Nie, C. Ouyang, J. Chen, Z. Zhong, Y. Du, D. Liu, S. Shi, and M. Lei, Solid State Commun. **150**, 40 (2010).
[3] S. K. Martha, B. Markovsky, J. Grinblat, Y. Gofer, O. Haik, E. Zinigrad, D. Aurbach, T. Drezen, D. Wang, G. Deghenghi, and I. Exnar, J. Electrochem. Soc. **156**, A541 (2009).
[4] G. Li, H. Azuma, and M. Tohda, Electrochem. Solid-State Lett. **5**, A135 (2002).
[5] Y. Asari, Y. Suwa, and T. Hamada, Phys. Rev. B **84**, 134113 (2011).
[6] A. Yamada and S. Chung, J. Electrochem. Soc. **148**, A960 (2001).
[7] A. Yamada, Y. Kudo, and K. Liu, J. Electrochem. Soc. **148**, A1153 (2001).
[8] D. Wang, H. Buqa, M. Crouzet, G. Deghenghi, T. Drezen, I. Exnar, N.-H. Kwon, J. H. Miners, L. Poletto, and M. Grätzel, J. Power Sources **189**, 624 (2009).
[9] V. Aravindan, J. Gnanaraj, Y.-S. Lee, and S. Madhavi, J. Mater. Chem. A **1**, 3518 (2013).
[10] M. Gaberscek, R. Dominko, and J. Jamnik, Electrochem. Commun. **9**, 2778 (2007).

[11]R. Toft-Petersen, N. H. Andersen, H. Li, J. Li, W. Tian, S. L. Bud'ko, T. B. S. Jensen, C. Niedermayer, M. Laver, O. Zaharko, J. W. Lynn, and D. Vaknin, Phys. Rev. B **85**, 224415 (2012).

[12]B. B. Van Aken, J.-P. Rivera, H. Schmid, and M. Fiebig, Nature (London) **449**, 702 (2007).

[13]N. Wizent, G. Behr, F. Lipps, I. Hellmann, R. Klingeler, V. Kataev, W. Löser, N. Sato, and B. Büchner,J. Cryst. Growth **311**, 1273 (2009).

[14]N. Wizent, G. Behr, W. Löser, B. Büchner, and R. Klingeler, J. Cryst. Growth **318**, 995 (2011).

[15]J. M. Mays, Phys. Rev. **131**, 38 (1963).

[16]J. Li, W. Tian, Y. Chen, J. L. Zarestky, J. W. Lynn, and D. Vaknin, Phys. Rev. B **79**, 144410 (2009).

[17]P. Heitjans and J. Kärger, *Diffusion in Condensed Matter—Methods, Materials, Models* (Springer, Berlin, 2005).

[18]K. Nakamura, H. Ohno, K. Okamura, Y. Michihiro, T. Moriga, I. Nakabayashi, and T. Kanashiro, Solid State Ionics **177**, 821 (2006).

[19]D. Arcon, A. Zorko, R. Dominko, and Z. Jaglicic, J. Phys.: Condens. Matter **16**, 5531 (2004).

[20]A. Abragam, *The Principles of Nuclear Magnetism* (Clarendon Press, Oxford, 1961) .

[21]J. H. Ranicar and P. R. Elliston, Phys. Lett. A **25**, 720 (1967).